Highly Selective Oxygen Reduction to Hydrogen Peroxide on Carbon-Supported Single-Atom Pd Electrocatalyst

Nan Wang[a], Xunhua Zhao[b], Rui Zhang[a], Saerom Yu[b], Zachary H. Levell[b], Chunyang Wang[a], Shaobo Ma[a], Peichao Zou[a], Lili Han[a], Jiayi Qin[a], Lu Ma[c], Yuanyue Liu[b]*, Huolin L. Xin[a]*

a Department of Physics and Astronomy, University of California, Irvine, California 94720, United States

b Texas Materials Institute, The University of Texas at Austin, Austin, Texas 78712, United States

c National Synchrotron Light Source II, Brookhaven National Laboratory, Upton, New York 11973, United States

Correspondence should be addressed to: yuanyue.liu@austin.utexas.edu (Y.L.) and huolinx@uci.edu (H.L.X.)

KEYWORDS: Pd single-atom, Two-electron ORR, Hydrogen peroxide, Electrocatalysts, Density functional theory

ABSTRACT: Selective electrochemical two-electron oxygen reduction is a promising route for renewable and on-site H_2O_2 generation as an alternative to the anthraquinone process. Herein, we report a high-performance nitrogen-coordinated single-atom Pd electrocatalyst, which is derived from Pd-doped zeolitic imidazolate frameworks (ZIFs) through one-step thermolysis. High angle annular dark-field scanning transmission electron microscopy (HAADF-STEM) combined with X-ray absorption spectroscopy verifies atomically dispersed Pd atoms on nitrogen-doped carbon (Pd-NC). The single-atom Pd-NC catalyst exhibits excellent electrocatalytic performance for two-electron oxygen reduction to H_2O_2, which shows ~95% selectivity toward H_2O_2 and an unprecedented onset potential of ~0.8 V versus revisable hydrogen electrode (RHE) in 0.1 M KOH. Density functional theory (DFT) calculations demonstrate that the Pd-N_4 catalytic sites thermodynamically prefer *-O bond breaking to O-O bond breaking, corresponding to a high selectivity for H_2O_2 production. This work provides a deep insight into the understanding of the catalytic process and design of high-performance $2e^-$ ORR catalysts.

1. INTRODUCTION

H_2O_2, as a valuable and environmentally friendly oxidizing agent, is an important fundamental chemical that is widely applied in modern chemical engineering industries, energy carriers, and wastewater treatment [1-2]. It is currently synthesized through the energy-intensive and waste-demanding anthraquinone method in industry [3]. In addition, it generally needs transportation and storage of unstable/hazardous H_2O_2 solutions [4]. To enable on-demand and real-time applications, direct on-site production of H_2O_2 through an electrochemical two-electron ORR process using renewable energy source provides an attractive and highly promising alternative. However, since the $2e^-$ ORR pathway always suffers from the competition from its otherwise $4e^-$ counterpart towards H_2O [5], it is crucial to develop efficient and economically viable catalysts with high activity and selectivity for ORR towards H_2O_2 instead of H_2O.

Single-atom catalysts (SACs), owing to their 100% atom efficiency, unique catalytic performance, and a fully exposed active site towards various reactions, have attracted tremendous attention in catalysis fields. In recent years, SACs have received increasing attention for their particularly high activity and selectivity to produce H_2O_2 via the $2e^-$ ORR pathway [6-7]. Huang et al. reported that 31 SACs have the potential to simultaneously achieve high activity and selectivity toward H_2O_2 production via DFT calculation. They further screened out 7 SACs with higher activity than the $PtHg_4$ in acidic media [7]. However, the selectivity and activity of SACs were unveiled only using DFT and machine-learning techniques rather than by experimental electrochemical measurements. Wang et al. reported different transition metal SACs combined with carbon nanotubes (Fe-CNT, Pd-CNT, Co-CNT, and Mn-CNT) via metal-C, O, or N coordination, and the Fe-CNT presented excellent electrocatalytic performance towards H_2O_2 generation in terms of activity and selectivity [8]. Other studies show that the underlying substrates can dramatically modify the electronic structure of supported single-atoms, thus altering the activity and selectivity of active sites [9-10]. For instance, the selectivity of single-atom Co from Co-NC is 80% [11-12], while both Co-PB-1(6) and Co-rPB-1(6) cages produce 90–100% H_2O_2 [13]. In addition, ZIFs can provide carbon and nitrogen supports to anchor atomically dispersed metal atoms [14]. It can overcome the high surface energy of single atoms that

restricts their fabrication [15]. Therefore, ZIFs have emerged as ideal precursors to synthesize various single-atoms, such as non-noble transition metals single atoms (Fe, Co, et. al) [16-17] and noble-metal single atoms (Ru, Ir, et. al) [18-19].

Noble metals, that generally exhibit advantages of high H_2O_2 catalytic activity, selectivity, and stability, are the most promising catalysts for the electrochemical production of H_2O_2 [20-24]. Pd-based carbon catalysts are often used for 2e$^-$ ORR and a low Pd loading and high interparticle distance may promote H_2O_2 selectivity [25-26]. Since Pd single-atom catalysts are generally synthesized on pure carbon materials, this easily leads to the formation of Pd clusters or nanoparticles due to aggregation. Therefore, it is necessary to fabricate high-performance, single-atom Pd electrocatalysts with low Pd loadings, while maintaining robust activity, high selectivity, and good durability.

Herein, we report a novel SACs synthesis method that enables efficient Pd loading within well-defined ZIF precursors to obtain atomically dispersed Pd single-atom catalyst on nitrogen-carbon (Pd_x-NC catalyst). The Pd_x-NC catalyst with optimized Pd doping content exhibit exceptional 2e$^-$ ORR activity and selectivity to produce H_2O_2 in alkaline media. Specifically, it shows ~95% selectivity toward H_2O_2 generation and an onset potential of ~0.8 V versus RHE in 0.1 M KOH. DFT calculations confirm that the Pd_x-NC catalyst thermodynamically prefers H_2O_2 (*-O breaking) to H_2O (O-O breaking) generation. Our work provides a novel SACs synthesis method and offers a new understanding of the 2e$^-$ ORR catalytic mechanism.

2. METHODS

2.1 Preparation and characterization of Pd single-atom catalysts

ZIF have been identified as ideal precursors to prepare M-N-C catalysts [27-31]. To prepare the Pd single-atom catalysts, Pd-doped ZIF precursors were firstly synthesized by varying the Pd content (Pd: Zn ratio) in methanol solution during ZIF crystal formation. The precursors are labeled as Pd_x-ZIF-8. Next, the precursors were calcinated at 900 °C for 2 hours under an argon atmosphere. The calcinated samples were labeled as Pd_x-NC, where n% (x varies from 0 to 1) is defined as Pd/Zn raw material mass ratio.

The morphology of Pd_x-ZIF-8 and Pd_x-NC were studied using scanning electron microscopy (SEM) on a Magellan 400 microscope at a working voltage of 10 kV. The morphology, elemental distributions, and atomic configurations of Pd_x-NC were characterized by a transmission electron microscopy (TEM) equipped with an energy dispersive X-ray spectroscopy (EDS) detector in the high-angle annular dark-field scanning TEM (HAADF-STEM) mode. The TEM was operated at 200 kV. X-ray photoelectron spectroscopy (XPS) was performed using a Kratos AXIS Ultra DLD XPS system equipped with a hemispherical energy analyzer and a monochromatic Al Kα source. All samples were prepared as pressed powders supported on zinc sheets for the XPS measurements. X-ray absorption spectroscopy (XAS) measurements at the Pd K-edge were carried out in the 7-BM beamline at National Synchrotron Light Source-II (NSLS-II) at Brookhaven National Laboratory. Inductively coupled plasma (ICP) was performed in iCAP RQ. Advanced first-principles calculations are performed to investigate the ORR thermodynamics at the solid-water interface of catalysts. The density functional theory calculations are performed with the Vienna Ab-initio Simulation Package (VASP). The calculation model and method are similar to those in the previous report [32]. The constrain ab initio molecular dynamics (AIMD) simulations are performed with atomic structure evolution using a slow-growth approach.

2.2 Electrochemical measurements

Electrochemical tests were performed using an CHI electrochemical workstation (CHI 730E) coupled with a rotating-ring disc electrode (RRDE, Pine) in a three-electrode cell. A graphite rod and a saturated calomel electrode (SCE) were used as the counter and reference electrodes, respectively. The reference electrode was calibrated to a reversible hydrogen electrode (RHE) in the same electrolyte before each measurement. A RHE was made with two Pt plates as working and counter electrodes to calibrate the SCE electrode and H_2 was bubbled over the working electrode. A rotating-ring disk electrode with a disk diameter of 5.6 cm covering a thin film of the catalyst was used work electrode. The electrocatalyst inks were prepared by dispersing samples in an isopropanol solution and Milli-Q (4:1) with 5 μL of Nafion (5%) to achieve the mass concentration of 5 mg mL^{-1} Pd_x-NC samples. Then 8 μL of each catalyst ink was drop-casted on a pre-cleaned glass carbon disk electrode and dried at room temperature to yield a thin-film electrode. The catalyst-coated disk working electrode was subjected to cyclic voltammetry (CV) at a scan rate of 50 mV s^{-1} in an Ar-saturated 0.1 M $HClO_4$, phosphate buffer solution (PBS), and KOH, respectively. The ORR catalytic activity was tested by rotating the disc electrode (RDE) in an O_2-saturated electrolyte solution (the solution resistance was compensated) at a scanning rate of 10 mV s^{-1} at 25 °C and a rotation rate of 1600 rpm. The electrochemical active surface area (ECSA) was estimated according to electrochemical double-layer capacitance (C_{dl}), based on the positive proportional relationship between ECSA and C_{dl} (ECSA = C_{dl} /C_s) [33], where C_s is the specific capacitance of carbon materials, and its real value is unknown. C_{dl} was determined by conducting CV with a 0.1 M KOH electrolyte solution with a potential range from -0.9 to 0.2 V vs SCE at increasing scan rates of 10, 50, 100, 150, 200, and 250 mV s^{-1} [34]. The value of C_{dl} was obtained from the slope of a derived plot of average current density at 1.0 V (vs RHE) vs. the scan rate. The average current density is equal to $(I_a+I_c)/2$, where I_a and I_c are the anodic current and the cathodic current, respectively, which can be read from the CV curves [35].

The ORR catalytic selectivity was tested by RRDE in an O_2-saturated electrolyte solution at a scanning rate of 10 mV s^{-1} at 25 °C and a rotation rate of 1600 rpm. The Pt-ring electrode was polarized at 1.4 V (vs RHE) to further oxidize the as-formed H_2O_2 from the disk electrode, and the collection efficiency of the ring electrode was calibrated to be 0.37. The electron transfer numbers and selectivity for the H_2O_2 yield were calculated using the following equations (eqs 1 and 2) according to the RRDE voltammogram of the catalysts.

$$n = \frac{4i_d}{i_d + i_r/N} \quad (1)$$

$$H_2O_2\% = 200 \times \frac{i_r/N}{(i_d + i_r/N)} \quad (2)$$

Where i_d is the disk current, i_r is the ring current, and N (N=0.37) is the current collection efficiency of the Pt-ring.

The catalyst stability was determined by chronoamperometry (CA) at 0.5 V (vs RHE) for 8 hours in O_2-saturated 0.1 M KOH solution at 25 °C and a rotation rate of 1600 rpm. Meanwhile, the Pt-ring electrode was polarized at 1.4 V (vs RHE).

An H-cell with a Nafion 117 membrane was used to confirm the selectivity of the Pd_x-NC electrocatalyst. Electrocatalysts were loaded on the glass carbon electrode. The concentration of the HO_2^- produced was measured by an iodometric titration, which method has been used to quantify the HO_2^- produced in previous reports [36]. In the experiment, 1.0 mL of the electrolyte was taken out from the chronoamperometry (at 0.5 V vs RHE for 6 h) reaction solution every 0.5 h. 0.5 mL of 2 % potassium iodide solution, 0.5 mL sulfuric acid, three drops of a molybdate catalyst and three drops starch solution, was added to a vial (H_2O_2 + 2KI + H_2SO_4 = I_2 + K_2SO_4 + 2H_2O), among starch as an indicator to determine the final endpoint. Then the above mixture solution was titrated with a thiosulfate solution of know concentration (I_2 + 2Na_2SO_4 = Na_2SO_4 + 2KI). When the characteristic blue color of the starch-iodine complex completely vanished to yield a clear solution, the endpoint was achieved.

3. Results and discussion

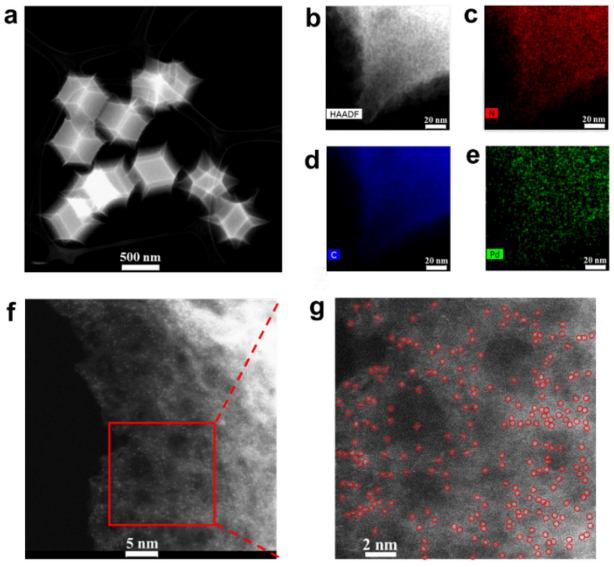

SEM imaging was performed to characterize and compare the morphologies of Pd_x-ZIF-8 and Pd_x-NC (Figure S1). The diameters of all the initial Pd_x-ZIF-8 are around 500 nm, which suggests an extremely small amount of Pd addition does not affect the specific structure of ZIF-8. In addition, when the pyrolysis process on Pd_x-ZIF-8 is conducted under an argon atmosphere, although the as-prepared Pd_x-NC exhibits slight shrinkage, the original rhomb dodecahedral shape and its size remain nearly the same. Figure 1a-g shows the structure and chemistry of $Pd_{0.157}$-NC catalyst with the best catalytic performance. The HAADF-STEM image (Figure 1a) shows that the substrate has a nearly ideal rhomb dodecahedral shape, implying that the volatilized zinc atoms do not change the organic molecular skeleton. In the synthesis process, the color of Pd_x-ZIF-8 precursor changes from white to black after high temperature (1173 K) pyrolysis process (Figure S3). In addition, no Pd nanoparticles were identified in the sample with low Pd loading. EDS mapping (Figure 1b-e) shows a nearly homogeneous elemental distribution of C, N, and Pd. To determine whether the Pd single-atom species in $Pd_{0.157}$-NC are atomically dispersed on the nitrogen-carbon support, atomic-resolution HAADF-STEM imaging was further conducted. The result (Figure 1f and 1g) shows that well-defined Pd single-atoms are formed and they distribute uniformly within the nitrogen-doped carbon support. Pd-containing nanoparticles were not observed in the $Pd_{0.157}$-NC with low Pd loading. However, for the Pd_x-NC with relatively higher Pd loading, Pd-rich nanoparticles are identified (Figure S2).

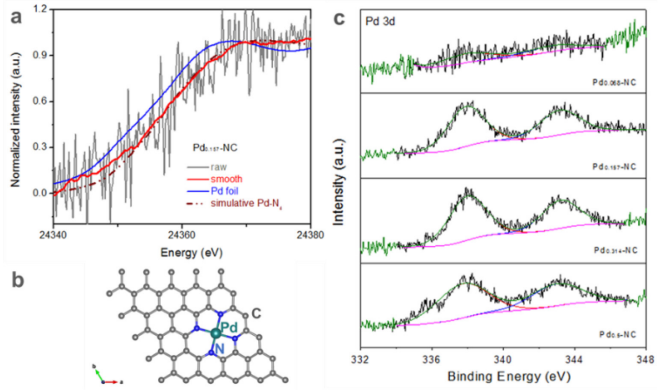

X-ray absorption near-edge structure (XANES) was performed to elucidate the local atomic structure of Pd atoms in Pd_x-NC. Figure 2a displays the normalized XANES of the Pd K-edge of $Pd_{0.157}$-NC and Pd foil. The smoothened curves of $Pd_{0.157}$-NC are plotted due to the weak absorption signal from the sample. Compared with Pd foil, the $Pd_{0.157}$-NC shows a higher Pd K-edge adsorption edge photon energy, indicating the Pd atoms in $Pd_{0.157}$-NC are in an oxidized state [37]. The measured XAS curve of $Pd_{0.157}$-NC catalyst is highly coincident with that of simulated Pd-N_4 substrate (Figure 2a and 2b), illustrating Pd in $Pd_{0.157}$-NC exists in the form of Pd-N_4 moiety. XPS was further performed to characterize the structure and electronic properties of Pd_x-NC. As shown in Figure 2c, the Pd 3d spectra from Pd_x-NC show two peaks in a 3:2 area ratio, which can be assigned to the $Pd_{5/2}$ and $Pd_{3/2}$ signals of a Pd^{2+} species. The Pd $3d_{5/2}$ feature centered at

337.7 eV is a fingerprint for Pd^{2+} [37]. In addition, the nitrogen content and the nitrogen speciation in Pd_x-NC were investigated (Figure S4 and Figure S5). Graphitic N (400.8 eV), pyrrolic N (400.0 eV), pyridinic N (398.2 eV), and Pd-N (397.7 eV) were identified [37-39]. Graphitic N, pyrrolic N, and pyridinic N in carbon frameworks can serve as anchor points for Pd single-atoms by forming Pd-N bonds [40]. Table S1 summarizes the types of N and their corresponding content. The loading contents of Pd in Pd_x-NC catalysts were measured by ICP (Table S2). The results show that the Pd contents in all the catalysts are less than 0.05%.

A steady-state linear sweep voltammetry (LSV) was performed to evaluate the ORR performance of the Pd_x-NC in 0.1 M KOH. NC catalyst (Pd_x-NC, x=0) without Pd loading was compared with Pd_x-NC catalysts with different Pd content. Figure 3a shows the polarization curves of Pd_x-NC catalysts, together with the H_2O_2 generation currents detected by the Pt ring electrode. The results (Figure 3a and S6a) show that NC has a higher onset potential compared with Pd_x-NC catalysts, and its' onset potential exceeds the limit potential (U_L = 0.8 V) for $2e^-$ ORR. The ORR catalytic kinetics was exposed by the Tafel plots (Figure S6b). The values of tafel slope follow the order of $Pd_{0.157}$-NC (56 mV Dec^{-1})< $Pd_{0.314}$-NC≈$Pd_{0.5}$-NC (71 mV Dec^{-1})<$Pd_{0.068}$-NC (73 mV Dec^{-1})<$Pd_{0.1}$-NC (78 mV Dec^{-1})<NC(80 mV Dec^{-1}). The corresponding electron transfer numbers and the H_2O_2 selectivity were calculated and plotted in Figure 3b as a function of potential. As shown in Figure 3b, the NC catalyst reveals an inferior H_2O_2 selectivity below 50% and the large electron transfer number around 3.0, implying that the NC catalyst catalyzes the ORR reaction via both the $2e^-$ route and the $4e^-$ route. Among those different Pd_x-NC catalysts, the $Pd_{0.157}$-NC catalyst shows the early onset potential of ~ 0.8 V (vs RHE) and H_2O_2 selectivity above 90%. These results confirm that the exceptional activity of Pd_x-NC catalysts mainly stems from the NC-supported Pd single-atoms sites. The effect of the Pd loading amount in the catalysts on the ORR catalytic performance was studied. As shown in Figure 3b, Pd_x-NC catalysts show excellent H_2O_2 selectivity, which is related to the Pd contents. The H_2O_2 generation selectivity of Pd_x-NC improves with the increase of the Pd loading, however, after a critical value, the H_2O_2 selectivity of Pd_x-NC starts to decrease. This is because Pd nanoparticles start to form with increased Pd loading (see details in Figure S2). Since Pd nanocrystals are favorable for $4e^-$ ORR to H_2O, they are detrimental to the $2e^-$ ORR [26]. The H_2O_2 selectivity of $Pd_{0.068}$-NC is lower than that of $Pd_{0.157}$-NC, due to the small amount of Pd single-atom in $Pd_{0.068}$-NC. When further increasing the Pd content in Pd_x-NC catalysts, $Pd_{0.157}$-NC, $Pd_{0.314}$-NC, and $Pd_{0.5}$-NC show high H_2O_2 selectivity (~90%), while the $Pd_{0.157}$-NC catalyst shows the best H_2O_2 selectivity performance (~95%). Generally, H_2O_2 as an intermediate can be further reduced to H_2O on the catalysts surface with high Pd loading content, as the strong absorption effect of Pd may increases the residence time of intermediates on the catalyst surface [26]. The above results suggest that the catalytic sites in $Pd_{0.157}$-NC catalyst is sufficient to optimize $2e^-$ ORR reaction, while the excessive Pd content will decrease H_2O_2 selectivity. In addition, the performance of the NC catalyst shows lower H_2O_2 selectivity compared to Pd_x-NC catalysts, which proves the Pd single-atoms play a key role in enhancing H_2O_2 selectivity and activity.

The Koutecky-Levich (K-L) analysis of Pd_x-NC catalysts was also carried out as an alternative to determine the H_2O_2 selectivity (Figure S7-11). Compared with the results obtained by the RRDE method, the K-L analysis results show a similar selectivity variation trend, but relatively higher selectivity for the Pd_x-NC catalysts with different Pd loadings. The overall higher selectivity by the K-L method is attributed to the fact that this method is only applicable to single-step reactions with a first-order dependence on the gas-phase reactant [41]. Therefore, for ORR with multistep pathways, the RRDE method is more reliable.

Figure 3c-d shows the electrocatalytic activity and H_2O_2 selectivity of $Pd_{0.157}$-NC tested in three electrolyte solutions with different pH values (0.1 M $HClO_4$, 0.1 M PBS, and 0.1 M KOH). As shown in Figure 3c, the $Pd_{0.157}$-NC catalyst exhibits distinguished catalytic performance in different solutions in the aspect of onset potentials and disk/ring current values. The disk current density in alkaline solution (0.1 M KOH) was far more than those in neutral and acidic solution. The variations of ring current density of the catalyst in different solutions are similar, implying the potential values can also influence H_2O_2 generation selectivity. As shown in Figure 3d, the $Pd_{0.157}$-NC catalyst shows an electron transfer number close to 2 and H_2O_2 selectivity above 90% in alkaline solution (0.1 M KOH) in the entire potential range of 0.1-0.7 V versus RHE. The H_2O_2 selectivity and electron transfer number in neutral (0.1 M PBS) and acidic solution (0.1 M $HClO_4$) are poorer than those in alkaline solution. These results show that the pH environment has also an effect on the activity and selectivity for H_2O_2 production.

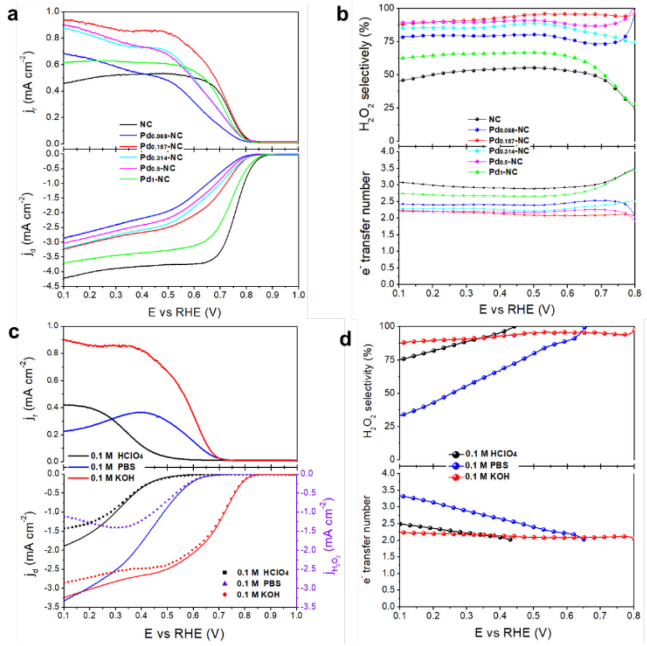

Figure 3 ORR performance of Pd_x-NC catalysts tested via RRDE. **a)** LSV of NC background and different ratio Pd_x-NC catalysts recorded in 0.1 M KOH at 1600 rpm and a scan rate of 10 mV s^-

[1], the ring electrode at a fixed potential of 1.4 V vs RHE. **b)** Calculated H_2O_2 selectivity and electron transfer number during a potential sweep. **c)** LSV of $Pd_{0.157}$-NC catalyst recorded in 0.1 M $HClO_4$, 0.1 M PBS, and 0.1 M KOH at 1600 rpm and a scan rate of 10 mV s^{-1}, the ring electrode at a fixed potential of 1.4 V vs RHE. **d)** Calculated H_2O_2 selectivity and electron transfer number during a potential sweep.

The mass activity (per catalyst) of reported 2e- ORR catalysts is compared with that of our prepared Pd_x-NC catalysts. As shown in Figure 4a, the synthesized Pd_x-NC catalyst with ultra-low Pd content delivers high mass activity, which is comparable to that of noble metal based catalysts [42]. ECSA is another important parameter to evaluate the electrocatalyst's activity and a large ECSA generally means high catalytic activity. The ECSA is estimated based on the positive proportional relationship between ECSA and C_{dl} [43-44], whereas C_{dl} is calculated from the different speed scan CV curves in 0.1 M KOH (Figure S12). In Figure 4b, the $Pd_{0.157}$-NC (5.11 mF cm^{-2}), $Pd_{0.314}$-NC (5.08 mF cm^{-2}), and $Pd_{0.5}$-NC (5.13 mF cm^{-2}) possess almost the same C_{dl} values, which are larger than that of the $Pd_{0.068}$-NC (4.48 mF cm^{-2}) and NC (4.40 mF cm^{-2}). The observed trend of C_{dl} is consistent with that of the ORR activity and H_2O_2 selectivity. It is worth noting that the $Pd_{0.5}$-NC with the largest ECSA does not exhibit the highest H_2O_2 selectivity due to the formation of Pd nanoparticles which makes it more favorable to H_2O generation via 4e- ORR pathway. In contrast, $Pd_{0.157}$-NC with 5.11 mF cm^{-2} ECSA exhibits the highest H_2O_2 selectivity compared with $Pd_{0.314}$-NC (5.08 mF cm^{-2}) and $Pd_{0.5}$-NC (5.13 mF cm^{-2}). These results indicate that the prepared Pd_x-NC catalyst with optimized Pd content possesses high ECSA and 2e- ORR catalytic performance.

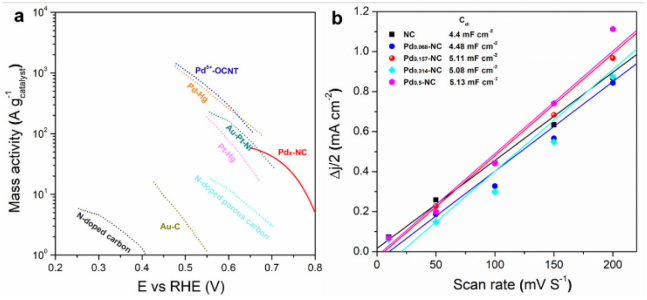

Figure 4 a) Mass activity of the state-of-the-art electrocatalysts for H_2O_2 production in the acid (dashed lines) or alkaline (solid lines) electrolytes. Data was taken from previous reports [8,9,15,20,24,35,36] and **b)** Charge currents of the different ratio Pd_x-NC plotted as a function scan rate.

The stability of $Pd_{0.157}$-NC was studied at 0.5 V versus RHE in an O_2-saturated 0.1 M KOH under static and rotating conditions. The currents density of the disk and ring electrode remained stable for 8 h without obvious decay as shown in Figure 5a. The current density of the ring electrode slightly increased, which could be attributed to the gradually accumulated H_2O_2 in the electrolyte. The LSV curves of $Pd_{0.157}$-NC before and after the stability test were compared (Figure S13). A slight change in the kinetic range might stem from the partial detachment of the catalyst from the electrode. In addition, the stability of $Pd_{0.157}$-NC was further confirmed by CV aging test for 10000 cycles (Figure S14). The amount of H_2O_2 generated in an H-cell (Figure S15) can be detected during the ORR process through titration method reported in previous work [45]. Figure 5b shows the accumulated amount of H_2O_2 normalized by Pd_x-NC over the reaction time in O_2-saturated 0.1 M KOH. It can be observed that the H_2O_2 production rate is related to the types of Pd_x-NC catalysts, and the changing trend is consistent with the H_2O_2 selectivity of the Pd_x-NC catalysts. Remarkably, the H_2O_2 production rate of ~30 mmol $g_{catalysts}^{-1}$ h^{-1} was less than that of reported nitrogen-doped carbon catalyst [46], which is attributed to the certain error from the titration method to detect H_2O_2 compared with the commercial H_2O_2 kit assay. In addition, the consecutive decomposition reaction of H_2O_2 was also a factor that affects the decrease of H_2O_2 production rate. Therefore, it is essential to study peroxide reduction reaction (PRR) to prove the high H_2O_2 production rate during the ORR process. In this respect, we studied the PRR activities of the catalysts in Ar-saturated 0.1 M KOH electrolyte no containing 1 mM H_2O_2 and containing 1 mM H_2O_2 (Figure S16) [12]. Almost no redox currents are detected in the control experiment without H_2O_2, implying no electrochemical redox reaction occurs. In the testing system with H_2O_2, the Pd_x-NC catalysts deliver significantly lower redox currents than NC catalyst, indicating the PRR is significantly suppressed on Pd_x-NC catalysts [47]. The above results confirm the effectiveness of Pd single-atoms on the NC support in suppressing the PRR. Compared with the previous reports, the synthesized Pd0.157-NC catalyst in this work delivers both high H_2O_2 yield (~95%) and onset potential (~0.8 V), indicating its attractive 2e- ORR catalytic performance (Table S3). Based on these results, it can be concluded that Pd_x-NC catalysts exhibit very distinct electrochemical properties for H_2O_2 production due to high ORR activity, high selectivity toward peroxide production, and low activity toward PRR.

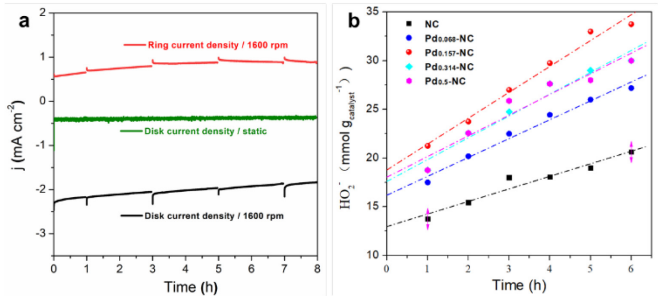

Figure 5 a) stability measurements of $Pd_{0.157}$-NC at a potential of 0.5 V vs RHE in O_2-saturated 0.1 M KOH and **b)** H_2O_2 production amount normalized to catalyst loading amount over the reaction time.

First-principles calculation based on density functional theory (DFT) was performed to investigate the catalytic mechanism, where Pd-N_4 embedded in graphene is used model the prepared Pd_x-NC SAC [39]. The H_2O_2 production selectivity on Pd-N_4/graphene substrate was studied using two thermodynamic models: the conventional computational hydrogen electrode model (CHEM) and the constant-potential model (CPM) [32, 48]. The CHEM often assumes the

system has zero surface charge, while in CPM the net electronic charges are balanced by ionic charges in the implicit solution implemented in the VASPsol patch [49]. Figure 6a displays the atomic structure of the *-O-OH bonded with Pd-N_4C catalytic site. Figure 6b reveals the free energies of every intermediate on Pd_x-NC catalyst. CHEM results shows *OOH formation has a thermodynamic barrier of 0.772 eV, while cp-CHEM predicts a 0.331 eV lower barrier, in agreement with the high onset potential observed in experiment. Moreover, the O-O bond breaking (*OOH → *O) thermodynamical barrier calculated by CHEM is significantly lower (0.304 vs 0.558 eV) than that by CPM. Nevertheless, both CHEM and CPM results indicate that, unlike Co-N_4 where the thermodynamics is not enough to explain the high H_2O_2 selectivity [6, 12, 32], the Pd-N_4 catalyst thermodynamically prefers *-O bond breaking than O-O bond breaking, implying the catalyst has a high selectivity for H_2O_2 production. The Pd-O bond at V_{RHE} = 0.7 V is 2.48 Å, in comparison with 1.89 Å of Co-O bond, while the O-O bond of *OOH is 0.07 Å shorter (1.37 vs 1.44) shorter than the counter part on Co-N_4. The relatively stronger O-O bond on Pd-N_4 indicats a larger kinetic barrier thus lower selectivity for the 4e path, and consequently higher 2e path (H_2O_2) selectivity. In addition, Pd(111) surface as a benchmark test is calculated using the same calculation models adopting for studying Pd-N_4. Figure 6c displays the top and side view of the configuration with *OOH intermediate on Pd(111) surface. The Figure 6d demonstrates the *-O bond breaking thermodynamic barrier calculated via CPM is lower than that of CHEM, which is consistent with the results in Figure 6b. Compared with the that of Pd-N_4, we find that Pd(111) shows a stronger oxygen binding energy. These calculation results show that Pd-N_4 exhibit high 2e path (H_2O_2) selectivity.

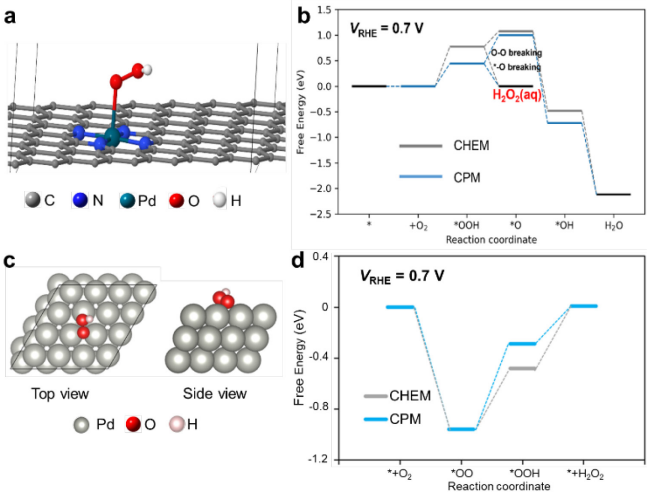

Figure 6 a) Atomic model structure of the *-O-OH bonded with Pd-N_4 C catalytic site, b) Free energy diagrams of the ORR on Pd-N_4 C, calculated using different models. c) Top and side view of the configuration with *OOH intermediate on Pd(111) catalyst. d) A free energy diagram for two-electron oxygen reduction reaction on Pd(111) at 0.7 V_{RHE}.

4. Conclusions

In summary, we demonstrate a novel Pd_x-NC single-atom catalyst synthesized by thermolysis of Pd doped ZIF precursors. The Pd-N coordination is crucial to forming atomically dispersed Pd SAC catalysts with high selectivity and activity of 2e⁻ ORR. The influence factors to 2e⁻ ORR catalytic performance are explored in detail, including Pd doping contents in catalysts, pH, and polarization potentials. The prepared $Pd_{0.157}$-NC catalyst delivers ~95% selectivity toward H_2O_2 in a wide potential range of 0.1 to 0.8 V and an onset potential of ~0.8 V versus RHE in 0.1 M KOH. Meanwhile, it also presents good catalytic activity and selectivity for 2e⁻ ORR in neutral and acid media. In addition, the H_2O_2 yield rate of the $Pd_{0.157}$-NC tested in an H-cell remained excellent stability with no decrease of the H_2O_2 selectivity with 8 h testing. DFT calculations suggest the Pd-N coordination is vital for its high H_2O_2 selectivity, with preferential *-O bond breaking than O-O bond breaking in the thermodynamics. This work provides a novel synthesis of high-performance 2e⁻ ORR catalysts and deep insight into its catalytic mechanism.

ASSOCIATED CONTENT

Supporting Information
The Supporting Information is available free of charge via the Internet at http://pubs.acs.org.

Additional SEM images, additional Pd K-edge EXAFS spectra, additional XPS spectra, ICP data and additional electrochemical data of Pd_x-NC (PDF).

AUTHOR INFORMATION

Corresponding Author

Yuanyue Liu − Texas Materials Institute, The University of Texas at Austin, Austin, Texas 78712, United States

Huolin L. Xin − Department of Physics and Astronomy, University of California, Irvine, California 94720, United States

Authors

Nan Wang − Department of Physics and Astronomy, University of California, Irvine, California 94720, United States

Xunhua Zhao − Texas Materials Institute, The University of Texas at Austin, Austin, Texas 78712, United States

Lili Han − Department of Physics and Astronomy, University of California, Irvine, California 94720, United States

Saerom Yu − Texas Materials Institute, The University of Texas at Austin, Austin, Texas 78712, United States

Zachary H. Levell − Texas Materials Institute, The University of Texas at Austin, Austin, Texas 78712, United States

Chunyang Wang − Department of Physics and Astronomy, University of California, Irvine, California 94720, United States

Shaobo Ma − Department of Physics and Astronomy, University of California, Irvine, California 94720, United States

Jiayi Qin − Department of Physics and Astronomy, University of California, Irvine, California 94720, United States

Rui Zhang − Department of Physics and Astronomy, University of California, Irvine, California 94720, United States

Lu Ma − National Synchrotron Light Source II, Brookhaven National Laboratory, Upton, New York 11973, United States

Notes

The authors declare no competing financial interest.

ACKNOWLEDGMENT

The synthesis, electrochemistry, and characterization done by the UCI team were supported by the National Science Foundation (NSF) under grant number CHE-1900401 and the startup funding of H.L.X. provided by UC Irinve. The theory work is supported by the NSF (Grant Nos. 1900039, 2029442), ACS PRF (60934-DNI6) and the Welch Foundation (Grant No. F-1959-20180324). The computations used computational resources at National Renewable Energy Lab, XSEDE and TACC, the Center for Nanoscale Materials at Argonne National Lab, and the Center for Functional Nanomaterials at Brookhaven National Lab. This research used resources of 7-BM of the National Synchrotron Light Source II and resources of the Center for Functional Nanomaterials (CFN), both are U.S. Department of Energy (DOE) Office of Science User Facilities operated for the DOE Office of Science by Brookhaven National Laboratory under Contract No. DE-SC0012704. The authors acknowledge the use of facilities and instrumentation at the UC Irvine Materials Research Institute (IMRI), which is supported in part by the National Science Foundation through the UC Irvine Materials Research Science and Engineering Center (DMR-2011967). XPS work was performed using instrumentation funded in part by the National Science Foundation Major Research Instrumentation Program under grant no. CHE-1338173.

REFERENCES

1. Yang, S.; Verdaguer-Casadevall, A.; Arnarson, L.; Silvioli, L.; Čolić, V.; Frydendal, R.; Rossmeisl, J.; Chorkendorff, I.; Stephens, I. E. L., *ACS Catalysis* **2018,** 8 (5), 4064-4081.
2. Brillas, E.; Sirés, I.; Oturan, M. A., *Chemical Reviews* **2009,** 109 (12), 6570-6631.
3. Campos-Martin, J. M.; Blanco-Brieva, G.; Fierro, J. L. G., *Angewandte Chemie International Edition* **2006,** 45 (42), 6962-6984.
4. Chang, Q.; Zhang, P.; Mostaghimi, A. H. B.; Zhao, X.; Denny, S. R.; Lee, J. H.; Gao, H.; Zhang, Y.; Xin, H. L.; Siahrostami, S., *Nature Communications* **2020,** 11, 2178.
5. Wu, F.; Pan, C.; He, C. T.; Han, Y.; Ma, W.; Wei, H.; Ji, W.; Chen, W.; Mao, J.; Yu, P.; Wang, D.; Mao, L.; Li, Y., *Journal of the American Chemical Society* **2020,** 142 (39), 16861-16867.
6. Gao, J.; Yang, H. b.; Huang, X.; Hung, S.-F.; Cai, W.; Jia, C.; Miao, S.; Chen, H. M.; Yang, X.; Huang, Y.; Zhang, T.; Liu, B., *Chem* **2020,** 6 (3), 658-674.
7. Guo, X.; Lin, S.; Gu, J.; Zhang, S.; Chen, Z.; Huang, S., *ACS Catalysis* **2019,** 9 (12), 11042-11054.
8. Jiang, K.; Back, S.; Akey, A. J.; Xia, C.; Wang, H., *Nature Communications* **2019,** 10, 3997.
9. Sun, Y.; Silvioli, L.; Sahraie, N. R.; Ju, W.; Li, J.; Zitolo, A.; Li, S.; Bagger, A.; Arnarson, L.; Wang, X., *Journal of the American Chemical Society* **2019,** 141 (31), 12372-12381.
10. Shen, R.; Chen, W.; Peng, Q.; Lu, S.; Zheng, L.; Cao, X.; Wang, Y.; Zhu, W.; Zhang, J.; Zhuang, Z., *Chem* **2019,** 5 (8), 2099-2110.
11. Li, B.-Q.; Zhao, C.-X.; Liu, J.-N.; Zhang, Q., *Advanced Materials* **2019,** 31 (35), 1808173.
12. Sun, Y.; Silvioli, L.; Sahraie, N. R.; Ju, W.; Li, J.; Zitolo, A.; Li, S.; Bagger, A.; Arnarson, L.; Wang, X.; Moeller, T.; Bernsmeier, D.; Rossmeisl, J.; Jaouen, F.; Strasser, P., *Journal of the American Chemical Society* **2019,** 141 (31), 12372-12381.
13. Smith, P. T.; Kim, Y.; Benke, B. P.; Kim, K.; Chang, C. J., *Angewandte Chemie International Edition* **2020,** 59 (12), 4902-4907.
14. Wang, X. X.; Cullen, D. A.; Pan, Y. T.; Hwang, S.; Wang, M.; Feng, Z.; Wang, J.; Engelhard, M. H.; Zhang, H.; He, Y.; Shao, Y.; Su, D.; More, K. L.; Spendelow, J. S.; Wu, G., *Advanced Materials* **2018,** 30 (11), 1706758.
15. Han, A.; Wang, B.; Kumar, A.; Qin, Y.; Jin, J.; Wang, X.; Yang, C.; Dong, B.; Jia, Y.; Liu, J.; Sun, X., *Small Methods* **2019,** 3 (9), 1800471.
16. Song, X. K.; Chen, S.; Guo, L. L.; Sun, Y.; Li, X. P.; Cao, X.; Wang, Z. X.; Sun, J. H.; Lin, C.; Wang, Y., *Advanced Energy Materials* **2018,** 8 (27).
17. Yuan, S.; Zhang, J. W.; Hu, L. Y.; Li, J. N.; Li, S. W.; Gao, Y. N.; Zhang, Q. H.; Gu, L.; Yang, W. X.; Feng, X.; Wang, B., *Angewandte Chemie-International Edition* **2021,** 60 (40), 21685-21690.
18. Ji, S. F.; Chen, Y. J.; Zhao, S.; Chen, W. X.; Shi, L. J.; Wang, Y.; Dong, J. C.; Li, Z.; Li, F. W.; Chen, C.; Peng, Q.; Li, J.; Wang, D. S.; Li, Y. D., *Angewandte Chemie-International Edition* **2019,** 58 (13), 4271-4275.
19. Liu, Q. T.; Li, Y. C.; Zheng, L. R.; Shang, J. X.; Liu, X. F.; Yu, R. H.; Shui, J. L., *Advanced Energy Materials* **2020,** 10 (20).
20. Jiang, Y.; Ni, P.; Chen, C.; Lu, Y.; Yang, P.; Kong, B.; Fisher, A.; Wang, X., *Advanced Energy Materials* **2018,** 8 (31), 1801909.
21. Edwards, J. K.; Hutchings, G. J., *Angewandte Chemie International Edition* **2008,** 47 (48), 9192-9198.
22. Yang, S.; Kim, J.; Tak, Y. J.; Soon, A.; Lee, H., *Angewandte Chemie International Edition* **2016,** 128 (6), 2098-2102.
23. Samira; Siahrostami; Arnau; Verdaguer-Casadevall; Mohammadreza; Karamad, *Nature Materials* **2013,** 12, 1137-1143.
24. Edwards, J. K.; Solsona, B.; Edwin, N. N.; Carley, A. F.; Herzing, A. A.; Kiely, C. J.; Hutchings, G. J., *Science* **2009,** 323 (5917), 1037-1041.
25. Wang, Y. L.; Gurses, S.; Felvey, N.; Boubnov, A.; Mao, S. S.; Kronawitter, C. X., *ACS Catalysis* **2019,** 9 (9), 8453-8463.
26. Fortunato; Guilherme; V.; Pizzutilo; Enrico; Mingers; Andrea; M.; Kasian; Olga, *Journal of Physical Chemistry C* **2018,** 122 (28), 15878-15885.
27. Liu, B.; Shioyama, H.; Akita, T.; Xu, Q., *Journal of the American Chemical Society* **2008,** 130 (16), 5390-5391.
28. Furukawa, H.; Cordova, K. E.; M Oâ, K.; Yaghi, O. M., *Science* **2013,** 341 (6149), 1230444.
29. Tang, H.; Cai, S.; Xie, S.; Wang, Z.; Tong, Y.; Pan, M.; Lu, X., *Advanced Science* **2016,** 3 (2), 1500265.
30. Armel, V.; Hindocha, S.; Salles, F.; Bennett, S.; Jones, D.; Jaouen, F., *Journal of the American Chemical Society* **2017,** 139 (1), 453-464.
31. Wang, H.; Zhu, Q.-L.; Zou, R.; Xu, Q., *Chem* **2017,** 2 (1), 52-80.
32. Zhao, X.; Liu, Y., *Journal of the American Chemical Society* **2021,** 143 (25), 9423-9428.
33. Han, L.; Sun, Y.; Li, S.; Cheng, C.; Halbig, C. E.; Feicht, P.; Strasser, P.; Eigler, S.; Hübner, J., *ACS Catalysis* **2019,** 9 (2), 1283-1288.
34. Roman, D. S.; Krishnamurthy, D.; Garg, R.; Hafiz, H.; Cohen-Karni, T., *ACS Catalysis* **2020,** 10 (3), 1993-2008.
35. Jia, N.; Yang, T.; Shi, S.; Chen, X.; Chen, P., *ACS Sustainable Chemistry & Engineering* **2020,** 8 (7), 2883-2891.
36. Hyo; Won; Kim; Michael; B.; Ross; Nikolay; Kornienko; Liang; Zhang, *Nature Catalysis* **2018,** 1, 282-290.
37. Zhou, S.; Shang, L.; Zhao, Y.; Shi, R.; Waterhouse, G. I. N.; Huang, Y.-C.; Zheng, L.; Zhang, T., *Advanced Materials* **2019,** 31 (18), 1900509.
38. Yang, H.; Wu, Y.; Li, G.; Lin, Q.; Hu, Q.; Zhang, Q.; Liu, J.; He, C., *Journal of the American Chemical Society* **2019,** 141 (32), 12717-12723.
39. Chen, Y.; Ji, S.; Wang, Y.; Dong, J.; Chen, W.; Li, Z.; Shen, R.; Zheng, L.; Zhuang, Z.; Wang, D.; Li, Y., *Angewandte Chemie International Edition* **2017,** 56 (24), 6937-6941.
40. Zhang, W.; Huang, H.; Li, F.; Deng, K.; Wang, X., *Journal of Materials Chemistry A* **2014,** 2 (44), 19084-19094.
41. Wei, C.; Rao, R. R.; Peng, J.; Huang, B.; Stephens, I. E. L.; Risch, M.; Xu, Z. J.; Shao-Horn, Y., *Advanced Materials* **2019,** 31 (31), 1806296.
42. Sheng, H.; Hermes, E. D.; Yang, X.; Ying, D.; Janes, A. N.; Li, W.; Schmidt, J. R.; Jin, S., *ACS Catalysis* **2019,** 9 (9), 8433-8442.
43. McCrory, C. C. L.; Jung, S.; Peters, J. C.; Jaramillo, T. F., *Journal of the American Chemical Society* **2013,** 135 (45), 16977-16987.
44. Han, L.; Yu, X.-Y.; Lou, X. W., *Advanced Materials* **2016,** 28 (23), 4601-4605.

45. Lu, Z.; Chen, G.; Siahrostami, S.; Chen, Z.; Liu, K.; Xie, J.; Liao, L.; Wu, T.; Lin, D.; Liu, Y., *Nature Catalysis* **2018,** 1 (2), 156-162.
46. Sun, Y.; Sinev, I.; Ju, W.; Bergmann, A.; Dresp, S.; Kühl, S.; Spöri, C.; Schmies, H.; Wang, H.; Bernsmeier, D.; Paul, B.; Schmack, R.; Kraehnert, R.; Roldan Cuenya, B.; Strasser, P., *ACS Catalysis* **2018,** 8 (4), 2844-2856.
47. Choi, C. H.; Kwon, H. C.; Yook, S.; Shin, H.; Kim, H.; Choi, M., *The Journal of Physical Chemistry C* **2014,** 118 (51), 30063-30070.
48. Zhao, X.; Liu, Y., *J Am Chem Soc* **2020,** 142 (12), 5773-5777.
49. Mathew, K.; Kolluru, V. S. C.; Mula, S.; Steinmann, S. N.; Hennig, R. G., *J Chem Phys* **2019,** 151 (23), 234101.

For Table of Contents Only